Research Article

Analysis of Multifrequency GNSS Signals and an Improved Single-Epoch RTK Method for Medium-Long Baseline

Jian Chen [1,2,3] **Jiahui Wang,** [1,2,3] **Kaikun Zhang,** [4] **Wei Duan,** [4] **Xingwang Zhao** [1,2,3] **and Chao Liu** [1,2,3]

[1]*School of Geomatics, Anhui University of Science and Technology, Huainan 232001, China*
[2]*Coal Industry Engineering Research Center of Mining Area Environmental and Disaster Cooperative Monitoring, Anhui University of Science and Technology, Huainan 232001, China*
[3]*Key Laboratory of Aviation-Aerospace-Ground Cooperative Monitoring and Early Warning of Coal Mining-Induced Disasters of Anhui Higher Education Institutes, Anhui University of Science and Technology, Huainan 232001, China*
[4]*Nanjing Institute of Surveying, Mapping & Geotechnical Investigation, Co. Ltd., Nanjing 211100, China*

Correspondence should be addressed to Jian Chen; 2020027@aust.edu.cn

In recent years, the quantity of visible satellites has increased significantly due to multiple satellite systems that leaped forward. The BeiDou Navigation Satellite System (BDS) and Galileo satellite navigation system (Galileo) broadcast triple-frequency signals and above to users, thus enhancing the reliability, continuity, and availability of the single-epoch real-time kinematic (RTK) positioning. In this study, an improved single-epoch multifrequency multisystem RTK method is successfully developed for the medium-long baseline. First, the Galileo and BDS extra-wide-lane (EWL) ambiguities are fixed at a high success rate, and the Galileo and BDS wide-lane (WL) ambiguity is achieved via the transformation process. Second, the fixed WL ambiguities of Galileo and BDS are exploited to elevate the fixed rate of GPS WL ambiguity. Third, the parametric strategies for ionospheric delay are carried out to upregulate the narrow-lane (NL) ambiguity-fixed rate of GPS. Further, the real-time data are adopted for verifying the feasibility of the method developed in this study. The experimental results demonstrate the optimal carrier-to-noise density ratio (C/N0) of full operational capability (FOC) E5a/E5b at all frequencies, followed by IIR-M L1, and IIR-A/B L2 exhibits the worst performance. Generally, the multipath combination (MPC) of Galileo signals shows root mean square (RMS) values within 0.4 m, ordered as follows: E1 > E5b > E5a. For the BDS-2, the B3 signal exhibits optimal performance, while the B1 signal is the worst. The RMS of MPC errors of L1 signals is smaller than the L2 signals for the GPS. Furthermore, under the 50 km baseline, the GPS NL ambiguity-fixed rate using the ionosphere-free (IF) combination reaches only 47.74% at the ratio threshold of 2. Finally, compared to the ionosphere-free combination method, the GPS NL ambiguity-fixed rate is increased by 45.52% with the presented method. The proposed approach broadens the future application of deformation monitoring in medium-long baseline scenarios.

1. Introduction

The Global Navigation Satellite System (GNSS) has been developed from the original Global Positioning System (GPS) into four primary systems, containing GPS, GLONASS, BDS, and Galileo systems. The GPS uses 31 satellites operating on Block IIR-A/B, IIR-M, IIF, and IIIF orbital planes. Apart from the L1 and L2 signals (1,575.420 and 1,227.600 MHz, respectively), the modernized GPS trans-mits the L5 signal (1,176.450 MHz) [1]. The GLONASS includes 23 satellites operating in orbit [2]. Currently, the total number of BDS operating constellations in orbit is 45, including 15 satellites in the BDS-2 and 30 satellites in the BDS-3 [3, 4]. Constellations are classified into three categories: geostationary orbit (GEO), inclined geosynchronous orbit (IGSO), as well as medium earth orbit (MEO) satellites. The BDS-2 transmits signals at B1, B2, and B3 frequencies (1,561.098, 1,207.140, and 1,268.520 MHz,
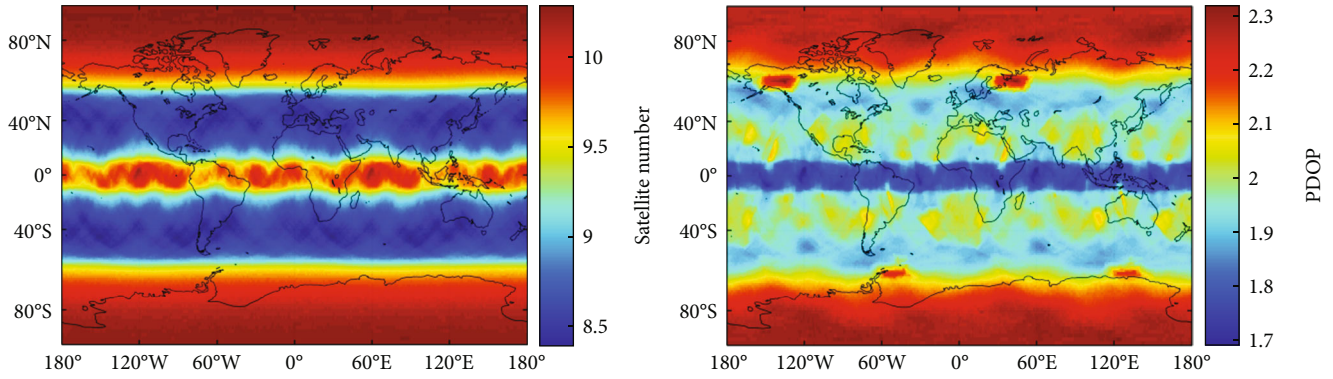
FIGURE 1: The quantity of satellite and PDOP for GPS at cutoff elevation of 10°.
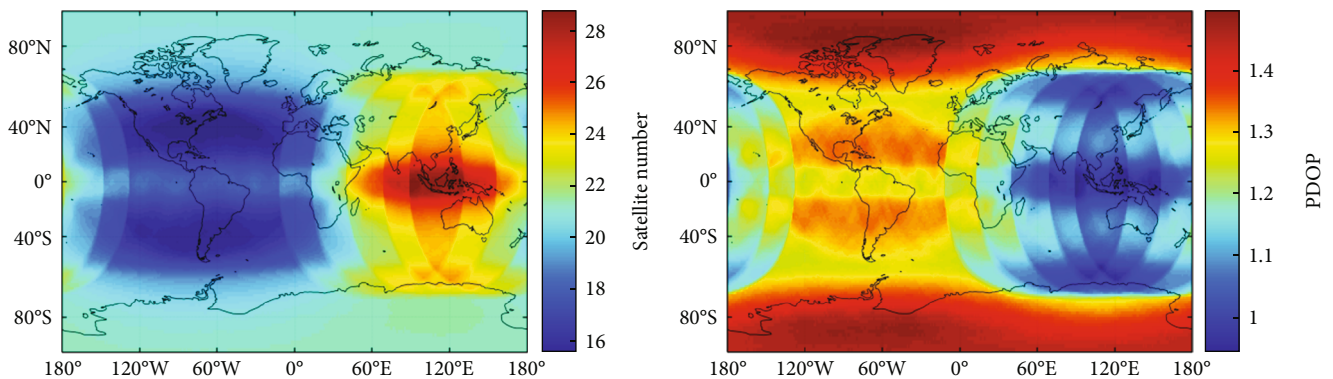

FIGURE 2: The quantity of satellite and PDOP for the combined Galileo/BDS-2/GPS at 10° cutoff elevation.

respectively). Aside from the B1 and B3 signals, the BDS-3 also broadcasts B1C, B2a, and B2b signals (1,575.42, 1,176.45, and 1,207.140 MHz, respectively). Currently, 23 Galileo satellites can be observed, in which 20 satellites are full operational capability (FOC) ones and 3 are in-orbit validation (IOV) ones. The Galileo broadcasts E1, E5, E5a, E5b, and E6 signals (1,575.420, 1,191.795, 1,176.450, 1,207.140, and 1,278.750 MHz, respectively) [5]. Due to its high accuracy, reliability, and availability, GNSS applications have been widely applied in fields such as land, ocean, aviation, and spatial [6–8].

To determine the optimal carrier linear combinations for multifrequency GNSS, scholars also put forward some algorithms, including the clustering analysis method [9, 10], analytical method [11], etc. The frequency division multiple access (FDMA) technique is used in GLONASS, whereas the code division multiple access (CDMA) technique is employed in GPS, BDS, and Galileo. For this reason, the current research considers only CDMA satellite systems to achieve single-epoch real-time kinematic (RTK) with multiple frequencies and systems. Figures 1 and 2 present the quantity of the satellites and the position dilution of precision (PDOP) of GPS and combined Galileo/BDS-2/GPS, respectively. These values range from 140 to 146 days in 2019 with the cutoff elevation set to 10°. As shown in Figures 1 and 2, in the combined Galileo/BDS-2/GPS system, the number of available satellites is three times that of the GPS,

with an average value of 25. The combined Galileo/BDS-2/GPS system has smaller PDOP values than the GPS. Accordingly, the increase in visible satellites can significantly enhance the geometry strength of the RTK-positioning model, which is conducive to the RTK resolution.

To achieve multi-frequency combined GNSS positioning, the least-squares ambiguity decorrelation adjustment (Lambda), cascading integer resolution (CIR), as well as triple-frequency carrier ambiguity resolution (TCAR) methods have been put forward successively [12–14]. Teunissen et al. [15] performed a systematic comparison of the fixed triple-frequency ambiguity for TCAR, CIR, and Lambda methods. The results indicated more superior performance of the Lambda approach than that of the CIR and TCAR models. The fixed rate of the narrow-lane (NL) ambiguity can be susceptible to atmospheric errors in the medium-long baseline. Feng [16] proposed the geometry-based (GB) TCAR method and achieved an optimal state and gave the optimal combined observations of GPS, Galileo, and BDS. Wang and Rothacher [17] introduced the pseudorange observations to construct a geometry-free and ionosphere-free (GIF) combination based on minimal noise and analyzed the applicability of the model for GPS, Galileo, and GLONASS. Nevertheless, the results indicated that this model had large noise when solving the NL ambiguity. Li et al. and Wu et al. [18, 19] exploited two fixed extra-wide-lane (EWL) ambiguities to calculate the ionospheric delay

TABLE 1: Specific information of the test data.

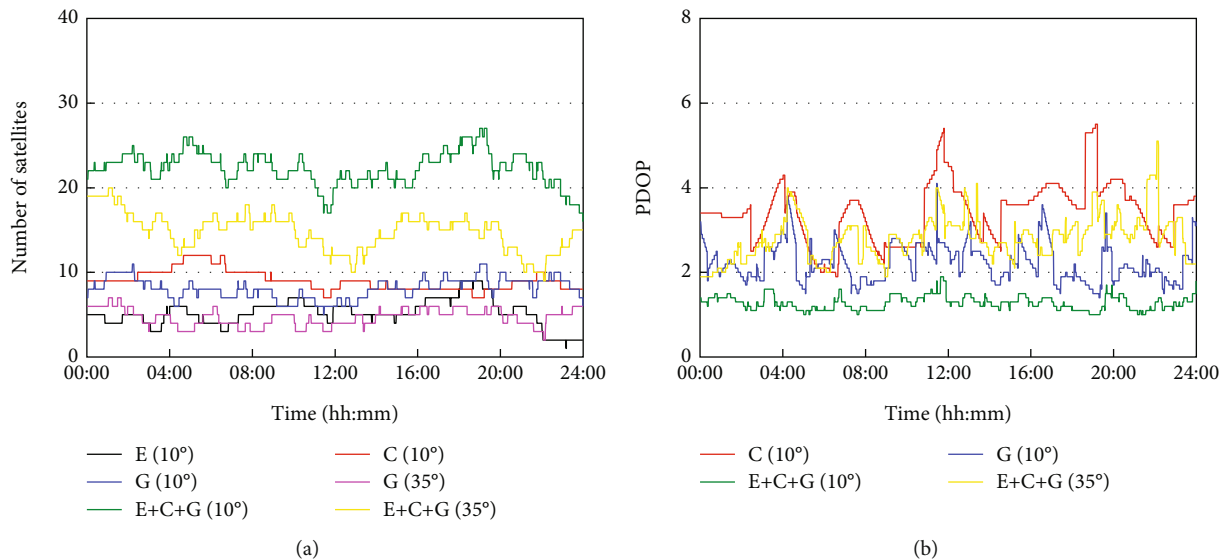| Dataset	Baseline	Baseline length (km)	Data	Sampling interval (s)	Receiver antenna type	Location
A	CUT0-PERT	22.41	DOY 10-16, 2019	30	TRIMBLE NETR9 TRM59800.00	Curtin University, Perth, Australia
B	CMDN-PDJP	30.20	DOY 142-148, 2019	10	CHC N71 HXCGG486A	Nanjing, China
C	FXTH-JPST	50.61	DOY 233-239, 2018	30	CHC N71 HXCGG486A	Shanghai, China

(a)

(b)

FIGURE 3: The visible satellite numbers and PDOP values of Galileo, BDS-2, GPS, and combined Galileo/BDS-2/GPS systems for the cutoff elevation of 10° and 35° at the FXTH station on August 21, 2018; labels "E," "C," "G," and "E + C + G" denote the Galileo, BDS-2, GPS, and combined Galileo/BDS-2/GPS systems, respectively.

to ameliorate the NL ambiguity-fixed rate. Under the condition of significant noise, the model should be smoothed for nearly 2 min to enhance the accuracy of ionospheric delay.

In the above results, the triple-frequency ambiguity resolution (AR) methods were theoretically analyzed, and the experiments were performed based on the simulated data. Triple-frequency data could be collected during the operation of the BDS-2 system. Tang et al. [20] compared the performances of the CIR and Lambda methods with the BDS-2 measured data and proposed a single-epoch solution model. To enhance the NL ambiguity-fixed rate for long distance, Li et al. [21] put forward the GIF model and found that the NL ambiguities were fixed over several minutes. After the ambiguity of WL and EWL was fixed, the ambiguity of NL could also be fixed rapidly using a partial ambiguity resolution (PAR) algorithm. Further, Zhang and He [22] tested the TCAR model, the Lambda method, and the GIF model using the triple-frequency data of BDS-2 and showed that the Lambda method with noncombined observations exhibited the best performance among all compared methods. In addition, it was verified that the GIF model could be easily affected by the multipath. Zhao et al. [23] developed an optimized TCAR model where the accuracy of the GIF combination was optimized by using fixed EWL and WL ambiguity, but the AR of NL was time-consuming. During the operation of BDS-3, the fixed ambiguity has been investigated for the new signal of BDS-3. Li et al. [24] introduced a linear combination of the BDS-3 B1C/B1I/B2a carrier phase observations. The numerical results obtained on real data show that the ionospheric-reduced combination (2, 2, -3) can reach 88.4% AR rate at a long baseline up to 1,600 km.

In terms of multi-GNSS combined positioning, before the development of the BDS system, the focus of multi-GNSS combinations primarily was placed on GLONASS and GPS systems. Al-Shaery et al. and Duan and Shen [25, 26] explored single GLONASS and combined GPS/GLONASS positioning, and the experimental data revealed higher RTK-positioning accuracy of the combined system compared to the corresponding value of a single system. With the official operation of the BDS system, combining the BDS with other existing satellite systems has become a research hotspot [27, 28]. The single-epoch GPS/BDS RTK was also investigated with respect to its positioning performance for a short baseline [29, 30], and the result illustrated that the GPS/BDS integrated system exhibited a remarkably higher success rate of the fixed ambiguity than the single GPS or BDS system. Teunissen et al. [31] reported that compared to a single system, the integrated GPS/BDS system could enhance the positioning accuracy and ambiguity resolution at the cutoff elevation of 40°. In addition, the
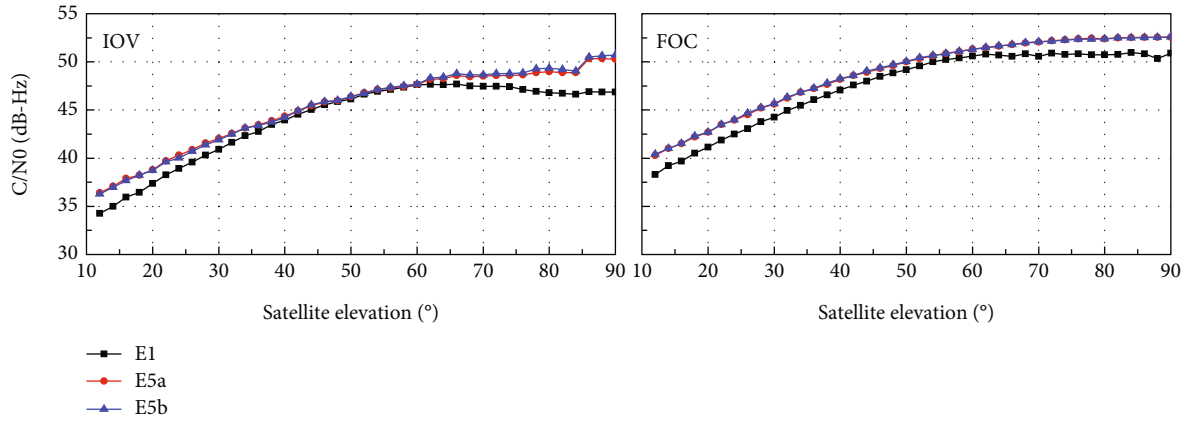
Figure 4: C/N0 values versus the satellite elevation for Galileo E1/E5a/E5b.
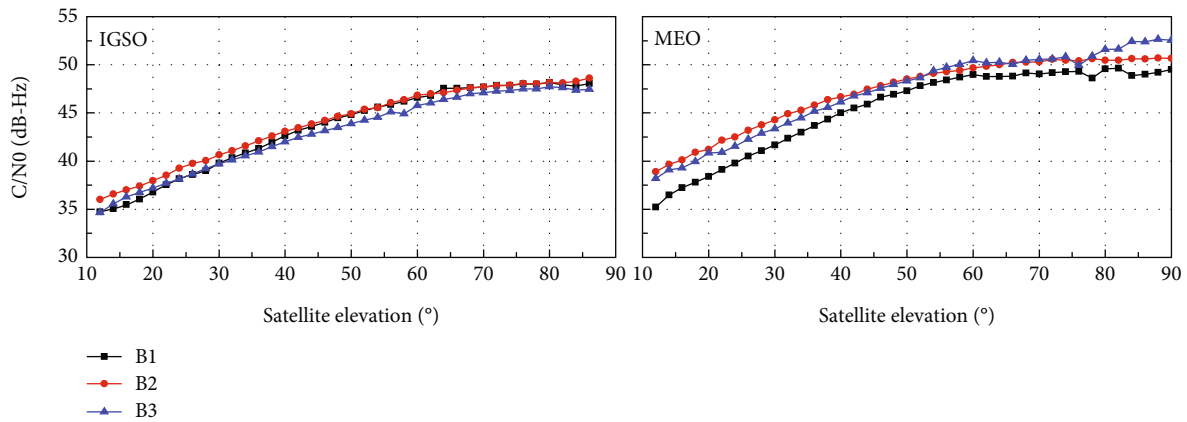

Figure 5: C/N0 values versus the satellite elevation for BDS B1/B2/B3.

positioning performance of single-frequency GPS/BDS/Galileo/QZSS RTK was evaluated by Odolinski et al. [32], and experiment data showed that the integer AR fixed rate of the integrated system was upregulated compared to the single, double, and triple systems. The related research has shown that a multisystem GNSS can enhance the strength of a parameter solution model and positioning availability, but combining systems could introduce certain problems (e.g., the introduction of low cutoff elevation angle satellites), which makes it more difficult to solve the ambiguity of all satellites simultaneously. On the basis of the cutoff elevation angle and ambiguity variance, Gao et al. and Wang and Feng [33, 34] formulated a strategy for the PAR, which enhanced the fixed rate of NL ambiguities significantly.

Generally, the EWL and WL integer ambiguity can be easier to fix by introducing multifrequency signals. However, under a medium-long baseline, the NL ambiguity is still difficult to fix correctly in a single epoch. Therefore, the ambiguity of NL observations requires further in-depth research. Given that, this study proposes an improved single-epoch multifrequency multisystem RTK method for the medium-long baseline. First, the Galileo and BDS EWL ambiguities are fixed at a high success rate, and the Galileo and BDS WL ambiguity is solved by the transformation process. Second, the ambiguity-fixed WL is adopted to upregulate the

WL ambiguity-fixed rate for the GPS combination observations, and a parameterizing strategy of the ionospheric delay is employed to enhance the fixed rate of GPS NL ambiguity. In addition, the availability of the proposed method is evaluated through real-time data.

The contents of the present work are summarized into the following sections: Section 2 shows the data collection process and signal quality analysis. In Section 3, a single-epoch RTK method of multifrequency positioning is presented, and the feasibility of the presented approach is evaluated experimentally. Finally, the main conclusions are drawn in Section 4.

2. Data Collection and Signal Quality Analysis

Observation data from two types of receivers (TRIMBLE NETR9 and CHC N71) were collected from three baselines. The CUT0-PERT baseline was located in the campus of Curtin University of Australia, and the data were acquired on January 10–16, 2019 (DOY 10-16, 2019). The CMDN-PDJP baseline was located in Nanjing, China, and data were harvested on May 22–28, 2019 (DOY 142-148, 2019). The FXTH-JPST baseline was located in Shanghai, China, and data were collected on August 21–27, 2018 (DOY 233-239, 2018). Three baseline lengths were 22.41 km, 30.20 km, and
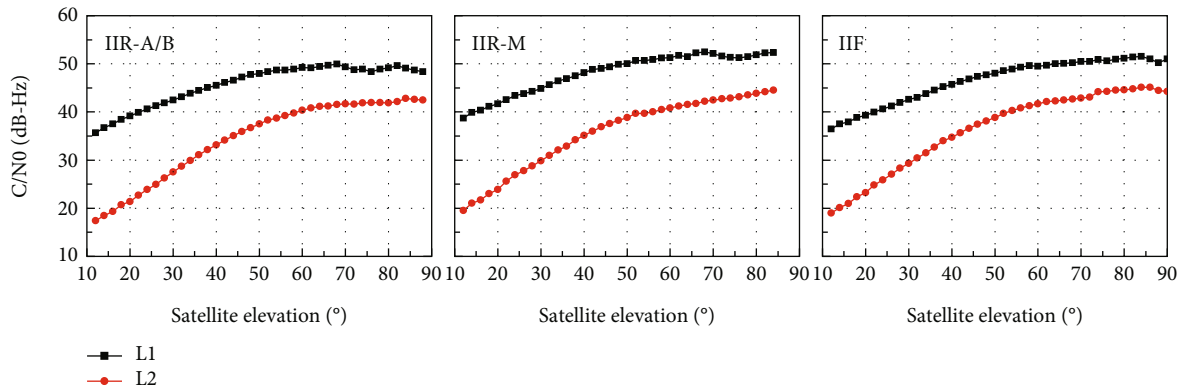
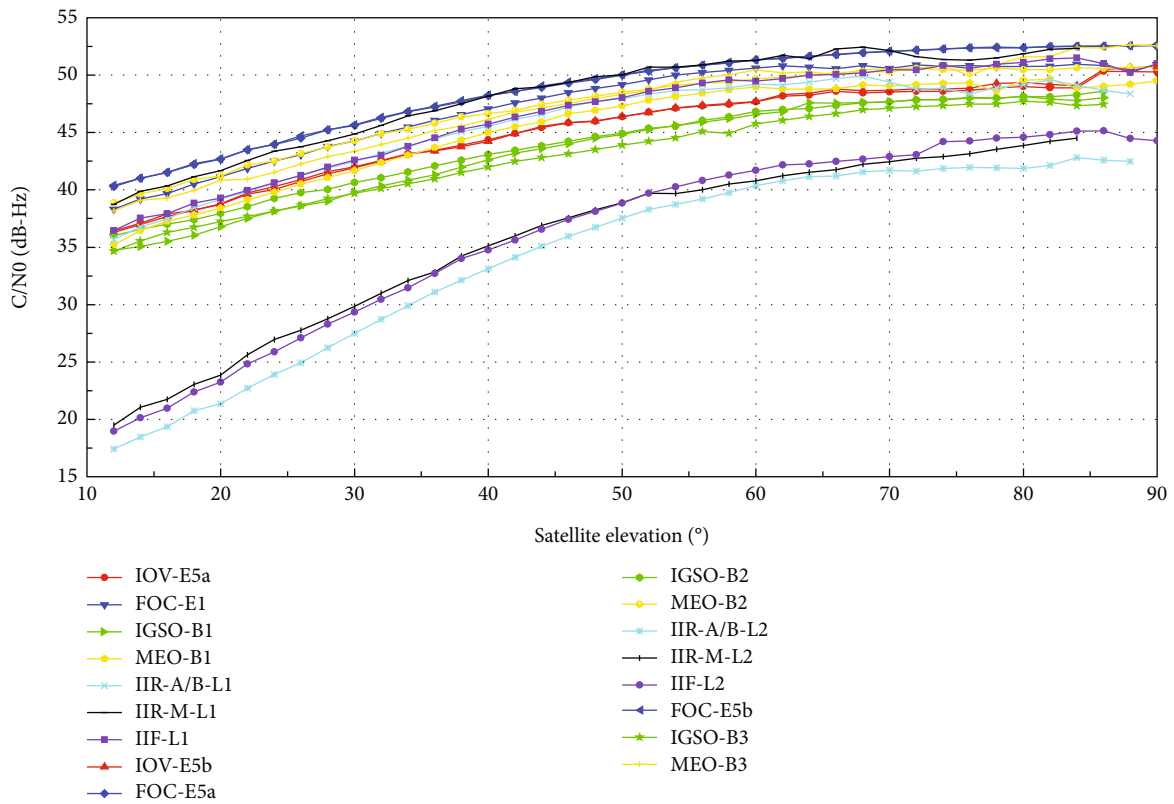Figure 6: C/N0 values versus the satellite elevation for GPS L1/L2.

Figure 7: C/N0 values versus the satellite elevation for satellites of varied types.

50.61 km, individually. The observations were harvested at a 30 s or 10 s sampling interval, and the cutoff elevation of 10° was applied. Table 1 provides more details on the baselines.

Figure 3 illustrates the time series of visible satellite number and PDOP for Galileo, BDS-2, GPS, and Galileo + BDS-2 + GPS combination with a 10° and 35° cutoff elevation angle at the FXTH station (August 21, 2018). As presented in Figure 3, in multiple epochs of the single Galileo system, there were fewer than 4 satellites at a cutoff elevation of 10°, which could not provide real-time positioning services. Also, the number of BDS-2 visible satellites was approximately 10 at the cutoff elevation of 10°, which was equal to the GPS satellite quantity. However, the BDS-2 system showed a higher PDOP value than the GPS, which was

mainly because the BDS-2 at this stage consists of GEO and IGSO (these GEO and IGSO covered the Asia-Pacific region). In addition, at a 10° cutoff elevation, the overall satellite quantity for the combined Galileo/BDS-2/GPS system was nearly 20, and the PDOP value was the lowest among all the systems, having a value of approximately 1.5. Accordingly, abundant satellites could enhance the satellite geometry strength, thus facilitating the RTK solution. Further, the number of single GPS at the 35° cutoff elevation was less than 4, while that of the combined Galileo/BDS-2/GPS system reached nearly 15, with the PDOP value of nearly 2. Thus, the significance of using the combined Galileo/BDS-2/GPS system could be mostly noticed in harsh environments (e.g., urban canyons).
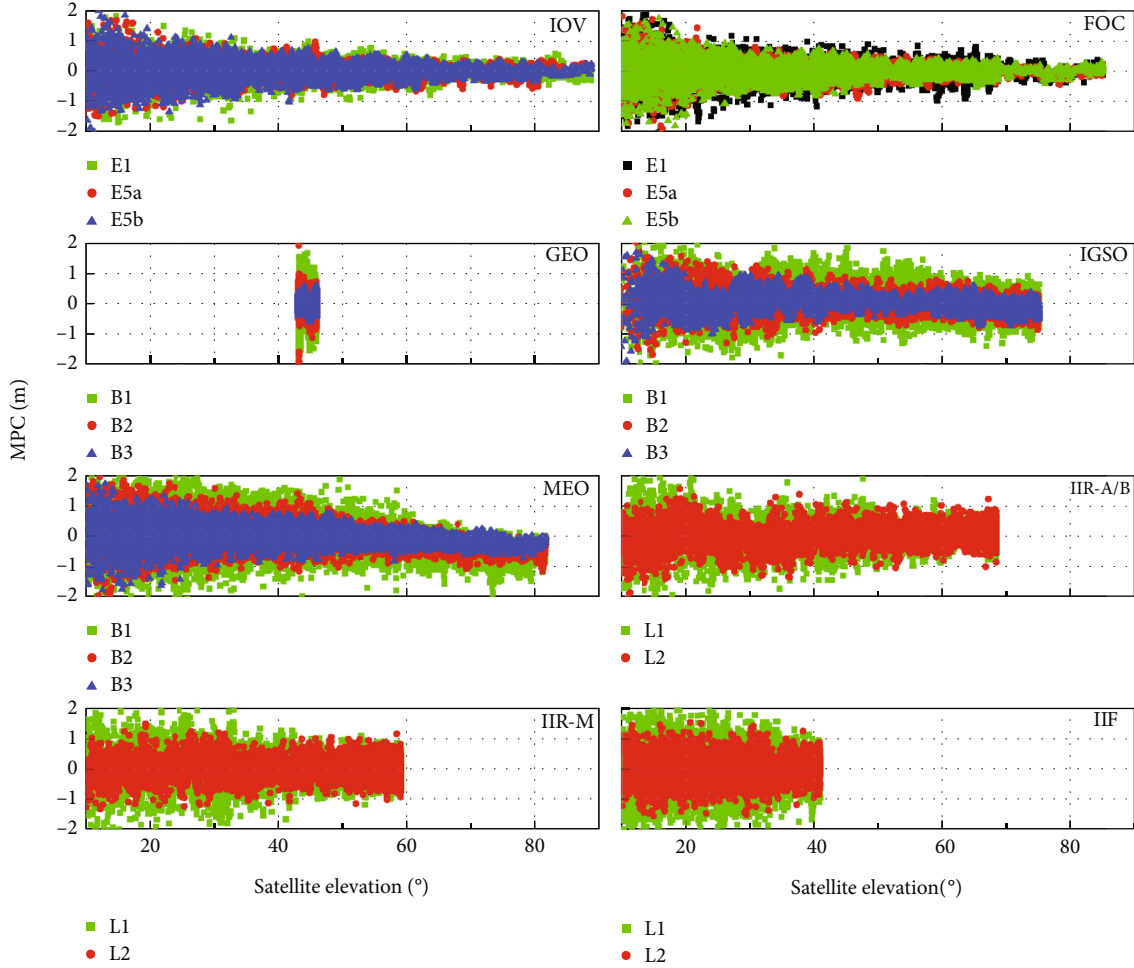
Figure 8: The MPC values versus the satellite elevation angle for different satellites at the CUT0 station with the Trimble NETR9 receiver collected on January 10–16, 2019.

Signal quality assessments were performed regarding the carrier-to-noise density ratio (C/N0) and the multipath combination (MPC) for the different signals. The observation results collected during seven days, on January 10–16, 2019, at CUT0 station, were used in the analysis. The higher C/N0 values correspond to better signal quality and higher observation accuracy. In the present study, the C/N0 data of the satellite signals were averaged based on 2° elevation intervals. Figure 4 shows the C/N0 data of Galileo signals concerning the elevation. It could be observed that a higher cutoff elevation resulted in larger C/N0 values. The C/N0 values of E5a and E5b signals were almost equal but better than those of the E1 signal for the identical type of satellite. At the identical cutoff elevation, the C/N0 values of FOC satellites were 2-3 dB-Hz larger than those of IOV satellites. The results of the three different signals in the BDS-2 system were presented in Figure 5. Since the elevation of GEO satellites varied slightly, the C/N0 value and cutoff elevation angle were not noticeably related, so their relation will not be presented in this paper. Figure 5 shows that C/N0 of B1, B2, and B3 signals for the IGSO satellites were basically the same. The C/N0 data of MEO satellite B2 and B3 signals were almost identical, 1-2 dB-Hz larger than that of the B1 signal at the identical cutoff elevation. Furthermore, the C/N0 values

for MEO satellites were 2-3 dB-Hz larger than those of IGSO satellites at the identical cutoff elevation. Therefore, it would be reasonable to consider that the elevation of the MEO satellites was remarkably lower compared to the corresponding value of IGSO satellites. Figure 6 gives the C/N0 values against the satellite elevation for GPS L1/L2. The C/N0 value of the L2 signal varied from 17 dB-Hz to 45 dB-Hz, and those of the L1 signal were from 35 dB-Hz to 52 dB-Hz. Thus, at the identical cutoff elevation, the C/N0 of the L1 signal for three types of satellites is noticeably higher than that of L2. According to the data of all the signals in Figure 7, the Galileo-FOC E5a/E5b exhibited the optimal performance at all frequencies, and it was followed by the IIR-M L1; the IIR-A/B L2 exhibited the worst performance. The Galileo-FOC satellite outperformed the other two systems mainly because of the application of advanced modulation schemes.

The MPC is commonly employed to assess pseudorange on a single-frequency observation. The MPC value can be obtained by

$$\mathrm{MPC}^s_{r*,j} = P^s_{r*,j} - \frac{f_j^2 + f_i^2}{f_j^2 - f_i^2} \Phi^s_{r*,j} + \frac{2f_i^2}{f_j^2 - f_i^2} \Phi^s_{r*,j} - B_{i,j}, \quad (1)$$
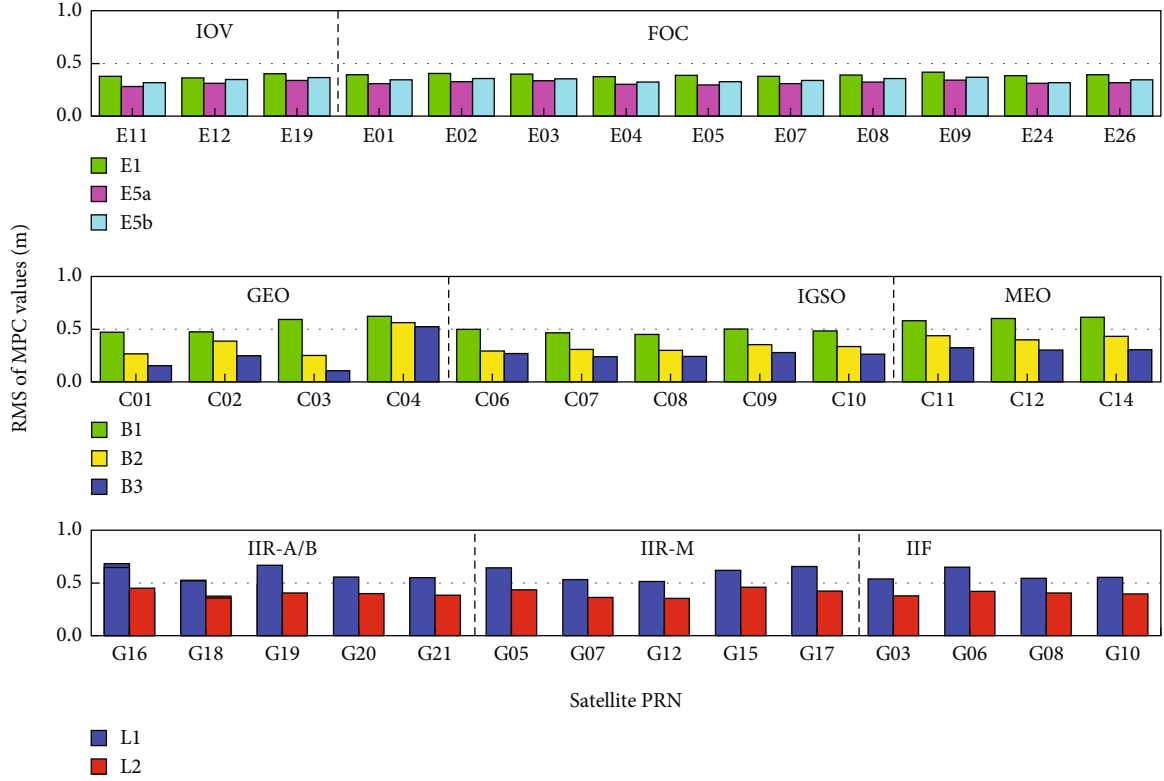
FIGURE 9: The RMS of the MPC for different satellites.

TABLE 2: EWL/WL combination characteristics for the triple-frequency BDS and Galileo systems.

(d, e, f)	$\lambda_{d,e,f}$ (m)	$\beta_{d,e,f}$	$u_{d,e,f}$	$\sigma_{\varphi_{d,e,f}}$ (cycle)	
				$\sigma_\varphi = 0.5$ cm	$\sigma_\varphi = 1$ cm
BDS (B1, B2, B3)					
(0, -1, 1)	4.884	-1.592	28.529	0.029	0.058
(1, 4, -5)	6.371	0.652	172.614	0.136	0.271
(1, -1, 0)	0.847	-1.293	5.575	0.033	0.066
(1, 0, -1)	1.025	-1.231	6.875	0.034	0.067
Galileo (E1, E5a, E5b)					
(0, -1, 1)	9.768	-1.748	54.923	0.028	0.056
(1, 5, -6)	1.396	-0.989	44.047	0.158	0.316
(1, -1, 0)	0.751	-1.339	4.928	0.033	0.066
(1, 0, -1)	0.814	-1.305	5.389	0.033	0.066

where $P_{r*,j}^s$ represents the pseudorange, $\Phi_{r*,j}^s$ indicates the carrier observations, r represents the receiver, s represents the satellite, f represents the carrier frequency, i and j represent the carrier frequency subscripts, * represents different systems, and $B_{i,j}$ stands for the integer-valued ambiguity.

IOV-E12, FOC-E04, GEO-C01, IGSO-C08, MEO-C11, IIR-A/B-G23 IIR-M-G12, and IIF-G06 satellites of the MPC values are given in Figure 8. As shown in Figure 8, the fluctuating range of the MPC values for different satellites was between -2 m and 2 m. Different from the GPS and Galileo systems, code biases existed in the BDS-2 sys-

tem. The GEO satellites were affected by the code bias, but for the small elevation interval, there was a slight correlation between the code bias and the cutoff elevation.

Figure 9 displays the RMS data of the MPC for each satellite type, in which the values of Galileo signals were mainly within 0.4 m, and the order was as follows: E1 > E5b > E5a. For BDS-2, the B3 signal exhibited the optimal performance, whereas the B1 signal performed the worst. For the GPS, the RMS values of the MPC for the L2 signal were smaller than those for the L1 signal.

3. Multifrequency Multisystem Ambiguity Resolution

Following the triple-frequency combination observation theory, the pseudorange combination coefficients are denoted as a, b, and c, while the carrier combination coefficients are represented by d, e, and f, and the observations of the double-difference combination could be indicated by the following equations:

$$\begin{aligned} \Delta P_{a,b,c} &= \frac{a \cdot f_1 \cdot \Delta P_1 + b \cdot f_2 \cdot \Delta P_2 + c \cdot f_3 \cdot \Delta P_3}{a \cdot f_1 + b \cdot f_2 + c \cdot f_3}, \\ \Delta \varphi_{d,e,f} &= \frac{d \cdot f_1 \cdot \Delta \varphi_1 + e \cdot f_2 \cdot \Delta \varphi_2 + f \cdot f_3 \cdot \Delta \varphi_3}{d \cdot f_1 + e \cdot f_2 + f \cdot f_3}, \end{aligned} \quad (2)$$

where Δ denotes the double-difference factor; φ_1, φ_2, and φ_3 refer to the carrier phase observations; P_1, P_2, and P_3 refer to
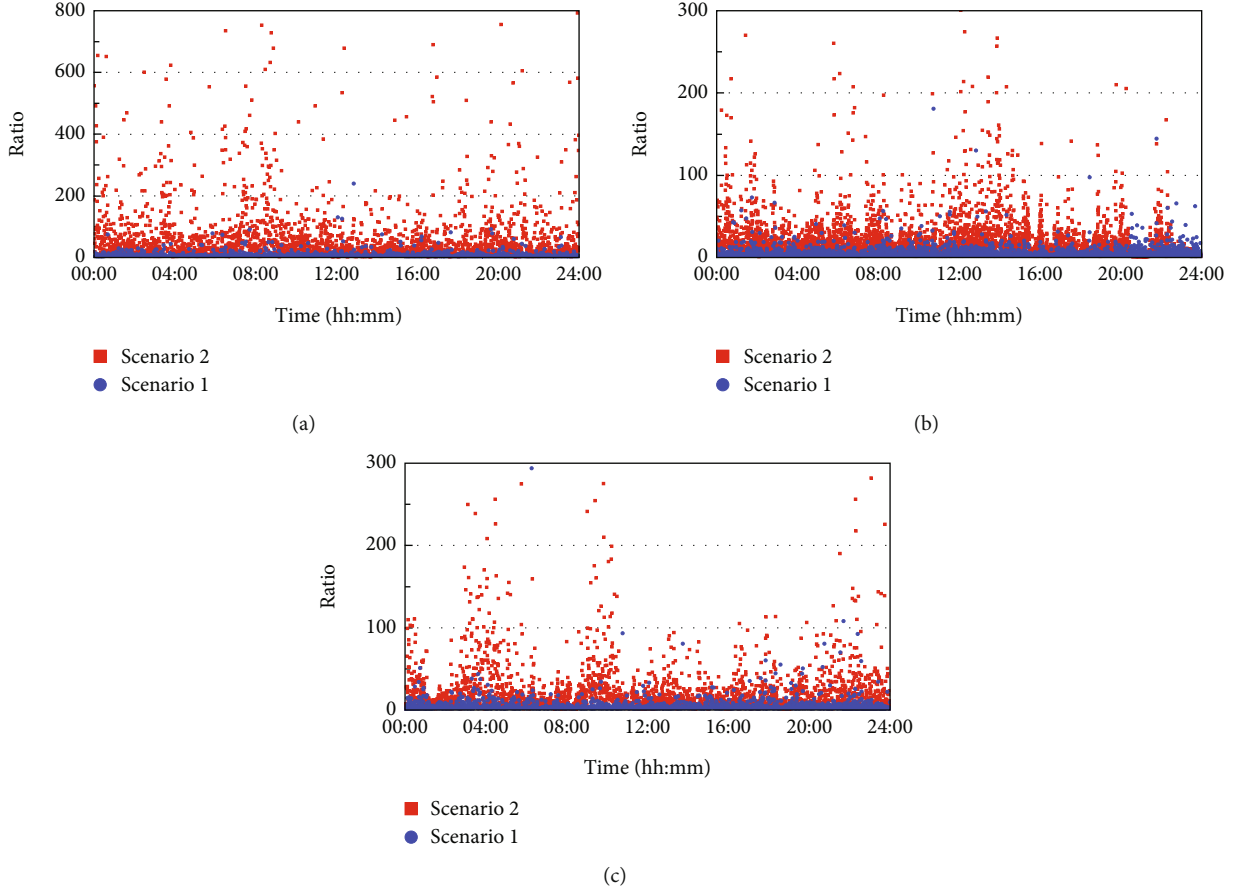
(a)

(b)

(c)

FIGURE 10: The AR performance of WL on datasets A, B, and C.

the pseudorange observations; and f_1, f_2, and f_3 represent the carrier phase observation frequencies.

The coefficient scale of first-order ionospheric delay $\beta_{d,e,f}$ and the noise coefficient scale $\mu_{d,e,f}$ of the combination observation are represented as

$$\beta_{d,e,f} = \frac{f_1^2(d/f_1 + e/f_2 + f/f_3)}{d \cdot f_1 + e \cdot f_2 + f \cdot f_3},$$

$$\mu_{d,e,f} = \frac{\sqrt{(d \cdot f_1)^2 + (e \cdot f_2)^2 + (f \cdot f_3)^2}}{d \cdot f_1 + e \cdot f_2 + f \cdot f_3}. \tag{3}$$

Over the past few years, optimal linear combinations with ionospheric-reduced delay, long wavelength, as well as low noise have been achieved for GNSS triple-frequency observations [35–37]. Table 2 lists the optimal combination characteristics of the triple-frequency observations for the BDS and Galileo systems.

3.1. EWL/WL Ambiguity Resolution. A medium-long baseline exhibits a large double-difference ionospheric delay, so the WL integer ambiguity-fixed rate is low. In our research, two sets of fixed EWL ambiguities were used for the determination of WL ambiguities through the linear transformation process. According to the characteristics of triple-frequency

TABLE 3: The WL ambiguity-fixed results for different scenarios.

Dataset	The integer ambiguity-fixed rate (%)			
	Ratio > 2		Ratio > 5	
	Scenario 1	Scenario 2	Scenario 1	Scenario 2
A	48.44	97.64	18.68	91.67
B	46.33	96.14	17.42	88.16
C	45.74	95.26	17.46	81.37

combination observation for the BDS and Galileo systems, the BDS system used (0, -1, 1) and (1, 4, -5), and the Galileo system used (0, -1, 1) and (1, 5, -6). The two sets of the EWL combination data were denoted by EWL1 and EWL2. Since the EWL1 had a longer wavelength, it was easy to fix. The observation equation derived using the EWL1 carrier observation and three pseudorange observations P_1, P_2, and P_3 are as follows:

$$\begin{bmatrix} v_{\text{EWL1}}^S \\ v_{P_1}^S \\ v_{P_2}^S \\ v_{P_3}^S \end{bmatrix} = \begin{bmatrix} \mathbf{B}^S & \lambda_{\text{EWL1}}^S \mathbf{I} \\ \mathbf{B}^S & 0 \\ \mathbf{B}^S & 0 \\ \mathbf{B}^S & 0 \end{bmatrix} \begin{bmatrix} \mathbf{X} \\ \mathbf{N}_{\text{EWL1}}^S \end{bmatrix} - \begin{bmatrix} \mathbf{I}_{\text{EWL1}}^S \\ \mathbf{I}_{P_1}^S \\ \mathbf{I}_{P_2}^S \\ \mathbf{I}_{P_3}^S \end{bmatrix}, \tag{4}$$
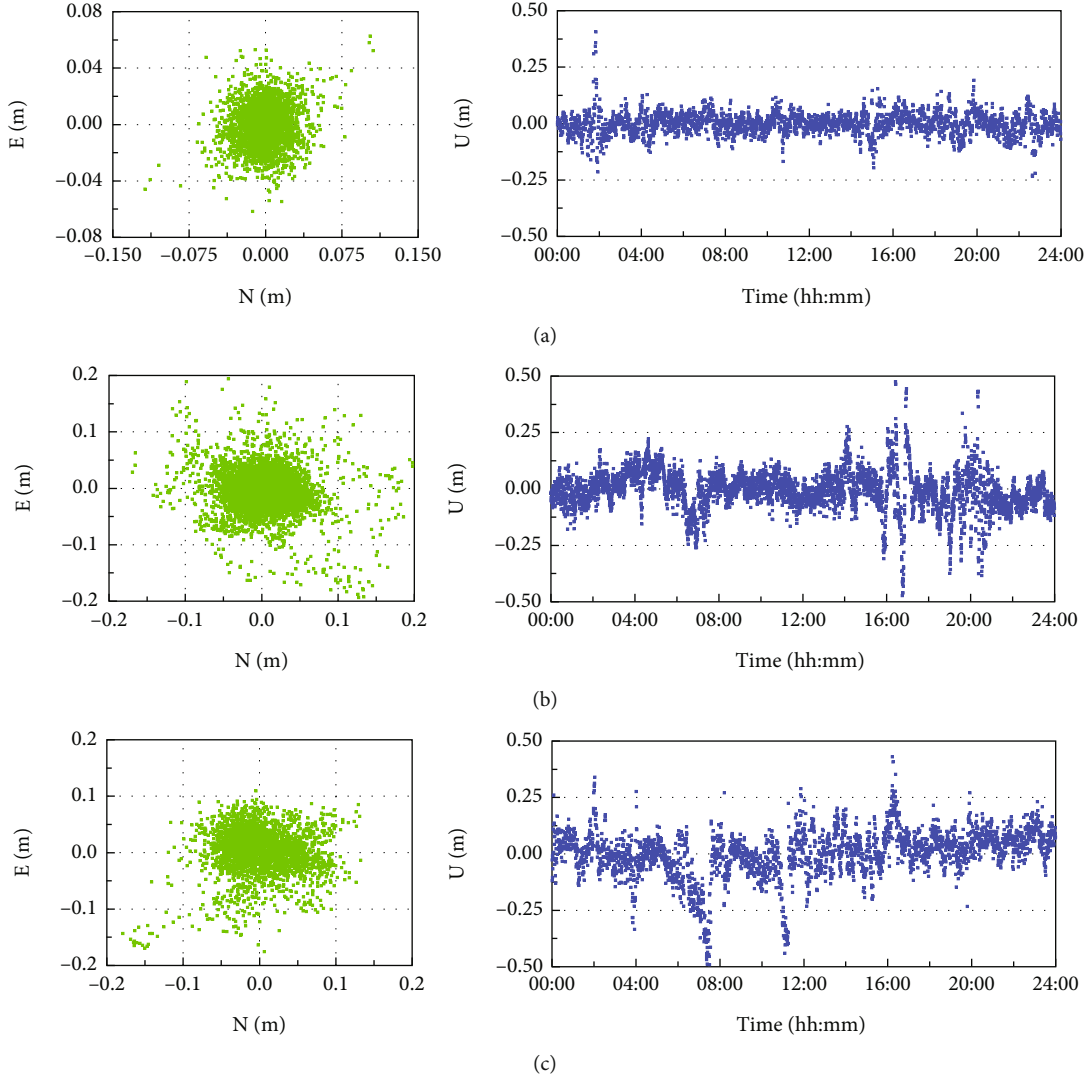
FIGURE 11: Time series of positioning errors for WL combination observations on datasets A, B, and C.

where a superscript S represents the BDS and Galileo; the coefficient matrix **B** corresponds to the positional vector parameters; v denotes the residual vector; **X** and **N** represent the baseline vector parameters and the ambiguity vector of carrier phase, respectively; and λ, **I**, and **l** are the wavelength of the EWL1 observation, identity matrix, and observed minus computed (OMC) vector of relevant observations, respectively.

The least-squares method was employed to obtain a floating solution of the ambiguity parameter, which was then fixed using the Lambda method. The EWL1 carrier observation and fixed EWL1 ambiguity could be considered a high-precision pseudorange observation. The EWL2 carrier observation can be expressed together with the EWL1 observation as follows:

$$\begin{bmatrix} v_{\text{EWL2}}^{S} \\ v_{\text{EWL1}}^{S} \end{bmatrix} = \begin{bmatrix} \mathbf{B}^{S} & \lambda_{\text{EWL2}}^{S}\mathbf{I} \\ \mathbf{B}^{S} & 0 \end{bmatrix} \begin{bmatrix} \mathbf{X} \\ \mathbf{N}_{\text{EWL2}}^{S} \end{bmatrix} - \begin{bmatrix} \mathbf{l}_{\text{EWL2}}^{S} \\ \mathbf{l}_{\text{EWL1}}^{S} \end{bmatrix}. \quad (5)$$

The EWL2 ambiguities were ascertained by the Lambda method. For the WL observations, both the BDS and Galileo

TABLE 4: Statistical data of positioning errors for WL observations (m).

Dataset	Direction N	Direction E	Direction U
A	0.021	0.015	0.048
B	0.039	0.037	0.088
C	0.041	0.039	0.106

systems adopted the (1, -1, 0) and (1, 0, -1) combination observations, which were recorded as WL12 and WL13, respectively. However, the GPS employed the (1, -1, 0) combination observations.

When the EWL ambiguity was fixed, the WL ambiguity of the BDS and Galileo can be determined by

$$\begin{aligned} N_{\text{WL12}}^{C} &= 5N_{0,-1,1} - N_{1,4,-5}, \\ N_{\text{WL13}}^{C} &= 4N_{0,-1,1} - N_{1,4,-5}, \\ N_{\text{WL12}}^{E} &= 6N_{0,-1,1} - N_{1,5,-6}, \\ N_{\text{WL12}}^{E} &= 5N_{0,-1,1} - N_{1,5,-6}, \end{aligned} \quad (6)$$
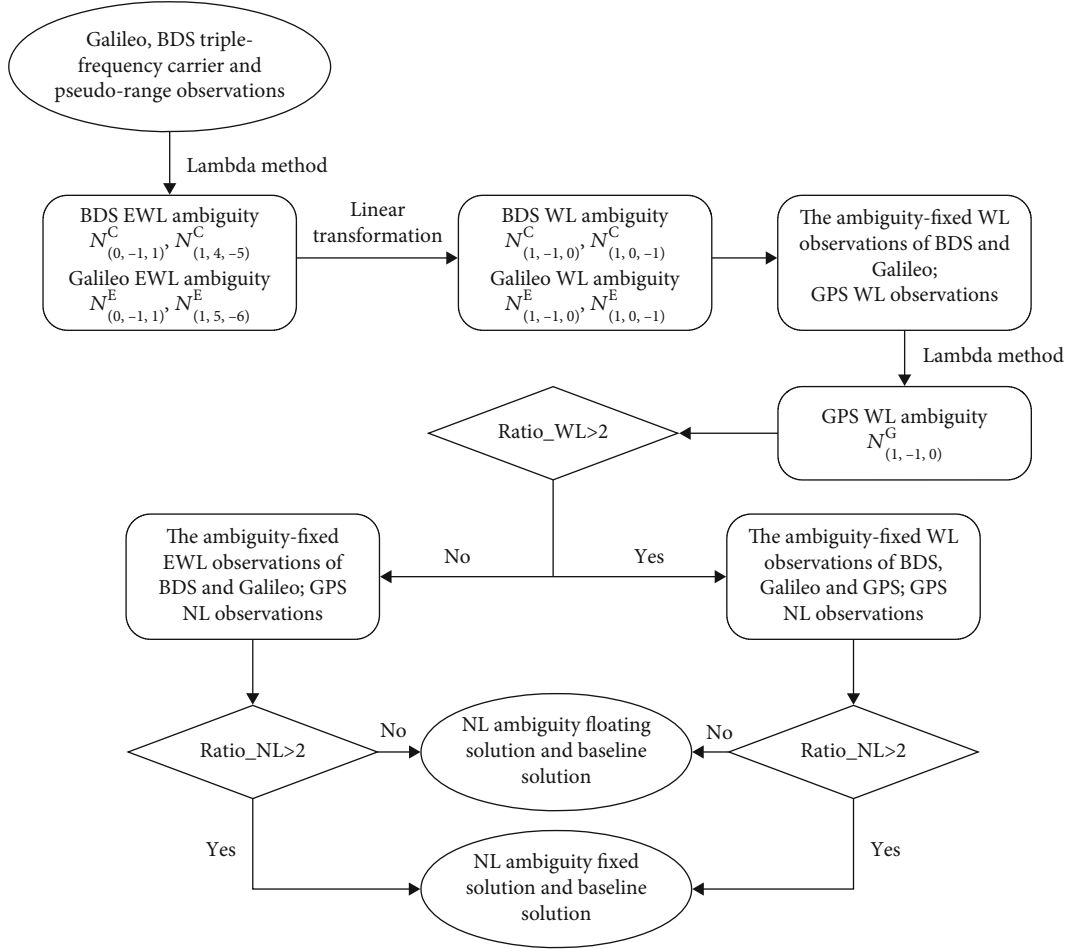
FIGURE 12: The multisystem multifrequency GNSS single-epoch RTK-positioning processing flow.

where C and E denote the BDS and Galileo systems, respectively.

The GPS exhibited a low WL ambiguity success rate under the medium-long baseline. In this study, the WL carrier observations with the fixed WL ambiguity of the BDS and Galileo systems were considered pseudorange observations. The GPS WL carrier observation can be described as follows:

$$
\begin{bmatrix}
v^{\mathrm{G}}_{\mathrm{WL12}} \\
v^{\mathrm{G}}_{P_1} \\
v^{\mathrm{G}}_{P_2} \\
v^{\mathrm{C}}_{\mathrm{WL12}} \\
v^{\mathrm{C}}_{\mathrm{WL13}} \\
v^{\mathrm{E}}_{\mathrm{WL12}} \\
v^{\mathrm{E}}_{\mathrm{WL13}}
\end{bmatrix}
=
\begin{bmatrix}
\mathbf{B}^{\mathrm{G}} & \lambda^{\mathrm{G}}_{\mathrm{WL12}}\mathbf{I} \\
\mathbf{B}^{\mathrm{G}} & 0 \\
\mathbf{B}^{\mathrm{G}} & 0 \\
\mathbf{B}^{\mathrm{C}} & 0 \\
\mathbf{B}^{\mathrm{C}} & 0 \\
\mathbf{B}^{\mathrm{E}} & 0 \\
\mathbf{B}^{\mathrm{E}} & 0
\end{bmatrix}
\begin{bmatrix}
\mathbf{X} \\
\mathbf{N}^{\mathrm{G}}_{\mathrm{WL12}}
\end{bmatrix}
-
\begin{bmatrix}
\mathbf{l}^{\mathrm{G}}_{\mathrm{WL12}} \\
\mathbf{l}^{\mathrm{G}}_{P_1} \\
\mathbf{l}^{\mathrm{G}}_{P_2} \\
\mathbf{l}^{\mathrm{C}}_{\mathrm{WL12}} \\
\mathbf{l}^{\mathrm{C}}_{\mathrm{WL13}} \\
\mathbf{l}^{\mathrm{E}}_{\mathrm{WL12}} \\
\mathbf{l}^{\mathrm{E}}_{\mathrm{WL13}}
\end{bmatrix},
\qquad (7)
$$

where a superscript G represents the GPS system and the rest of the labels have the same meaning as in Equation (4). After obtaining the floating solution of the WL ambi-

guity and its corresponding vc-matrix, the lambda method was adopted for fixing the ambiguity.

Two test scenarios were conceived to appraise the positioning performance of the single-epoch GNSS. In Scenario 1, the characteristic of the single GPS WL AR was evaluated, while in Scenario 2, the fixed rate of the GPS WL AR found on BDS/Galileo WL observations was analyzed. In the two scenarios, the Ratio threshold and the RMS value of the positioning errors were used to verify the ambiguity fixing reliability and positioning performance. The solution mode adopted the AR of the single epoch. In practical applications, single-epoch RTK-positioning solutions have rarely been used, and using the single-epoch analysis mode is more conducive to assessing the accuracy and feasibility of RTK. The Ratio was calculated by

$$
\mathrm{Ratio} = \frac{\left\| \hat{\mathbf{N}} - \breve{\mathbf{N}}_2 \right\|_{\mathbf{Q}_{\hat{\mathbf{N}}}}}{\left\| \hat{\mathbf{N}} - \breve{\mathbf{N}}_1 \right\|_{\mathbf{Q}_{\hat{\mathbf{N}}}}} \ge c,
\qquad (8)
$$

where $\hat{\mathbf{N}}$ denotes the float ambiguity resolution; $\breve{\mathbf{N}}_1$ and $\breve{\mathbf{N}}_2$ represent the minimum and second minimum of quadratic forms for ambiguity candidates, respectively; $\|\cdot\|_{\mathbf{Q}_{\hat{\mathbf{N}}}} = (\cdot)^{\mathrm{T}}$
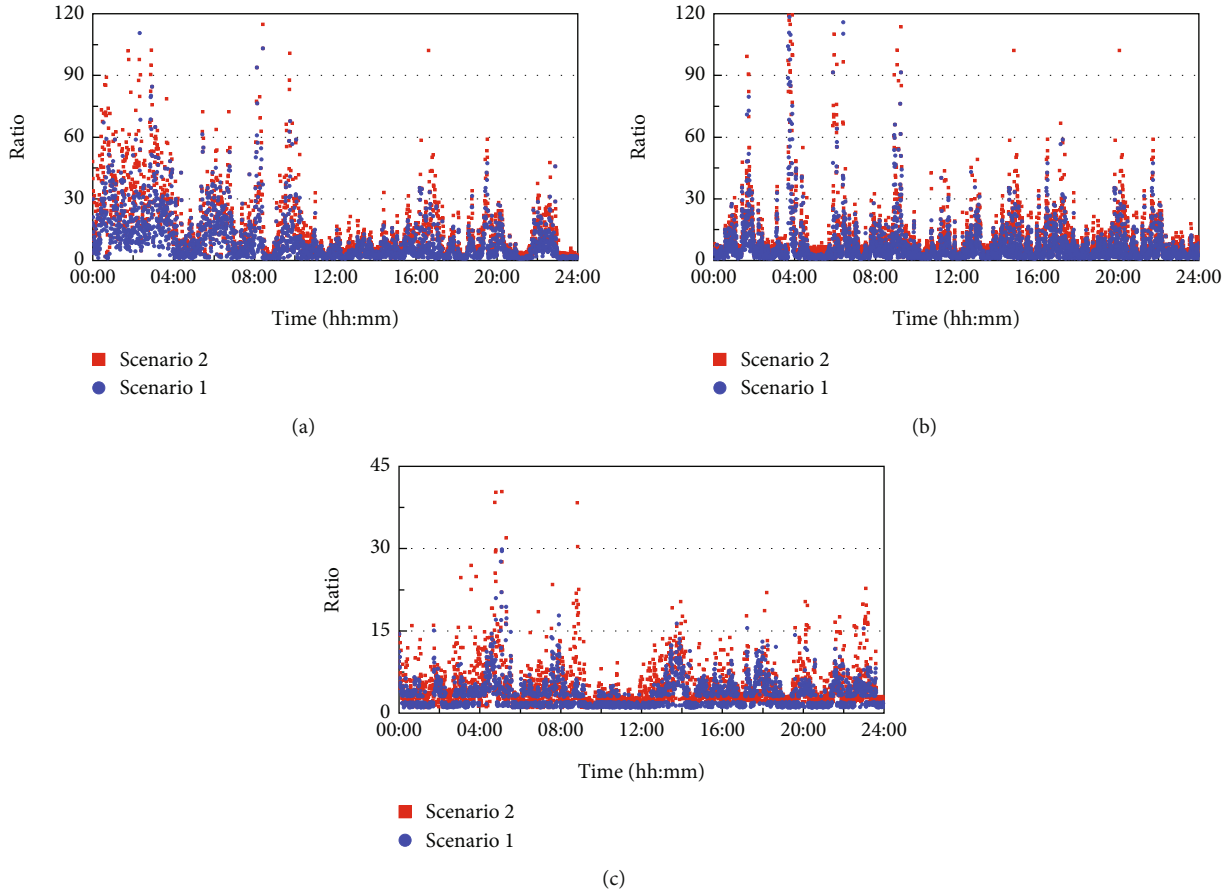
(a)

(b)

(c)

Figure 13: The AR performance of NL on datasets A, B, and C.

$\mathbf{Q}_{\hat{\mathbf{N}}}^{-1}(\cdot)$, where c is the threshold, which was set to 2 or 5. The Ratio values of scenarios 1 and 2 for the three baselines are presented in Figure 10. As observed from the figure, the Ratio values of Scenario 2 are noticeably higher compared to the relevant values of Scenario 1, demonstrating that Scenario 2 exhibited more excellent WL AR performance than Scenario 1. Table 3 lists the performance results of the two scenarios with respect to the single-epoch WL AR. At a Ratio value of 2, the maximal fixed rate of AR for Scenario 1 was only 48.44%, while the maximal fixed rate of AR for Scenario 2 was higher, having a value of 97.64%. Even at the 50 km baseline, at the Ratio value of 2, the fixed rate of the GPS WL AR for BDS/Galileo could reach a value over 95%. The Galileo/BDS WL carrier observations, together with the fixed WL ambiguity of the BDS and Galileo systems, could enhance the constraint strength of the model, which could help to upregulate the rate of GPS WL ambiguity fixing.

In addition to the single-epoch AR performance, the accuracy of RTK was also evaluated. The position errors of the single-epoch in the east (E), north (N), as well as up (U) directions for these 3 baselines are illustrated in Figure 11. As revealed from these figures, the GPS single-epoch WL observations showed positioning errors below 0.2 m in the E and N directions and below 0.5 m in the U direction. The positioning accuracies of the GPS WL obser-

Table 5: The NL ambiguity-fixed results for different scenarios.

Dataset	The integer ambiguity-fixed rate (%)			
	Ratio > 2		Ratio > 5	
	Scenario 1	Scenario 2	Scenario 1	Scenario 2
A	70.22	96.32	32.64	48.67
B	58.73	94.50	25.42	38.16
C	47.74	93.26	10.16	29.37

vations are listed in Table 4. The positioning accuracies of the horizontal and vertical directions are 0.03 and 0.05 m for dataset B, respectively. For the 50 km baseline, the RMS was approximately 0.04 m horizontally and 0.1 m vertically. Briefly, the WL observations could ensure subdecimeter positioning accuracy.

3.2. NL Ambiguity Resolution. For medium-long baselines, the fixed NL ambiguity is subject to the ionospheric delay. Although first-order ionospheric delay can be excluded through an ionosphere-free (IF) combination, its noise is amplified. In this study, the ionospheric delay error, ambiguity, and position are considered as unknown parameters. The Galileo/BDS/GPS WL ambiguities, together with the original carrier observations, can be used to derive the
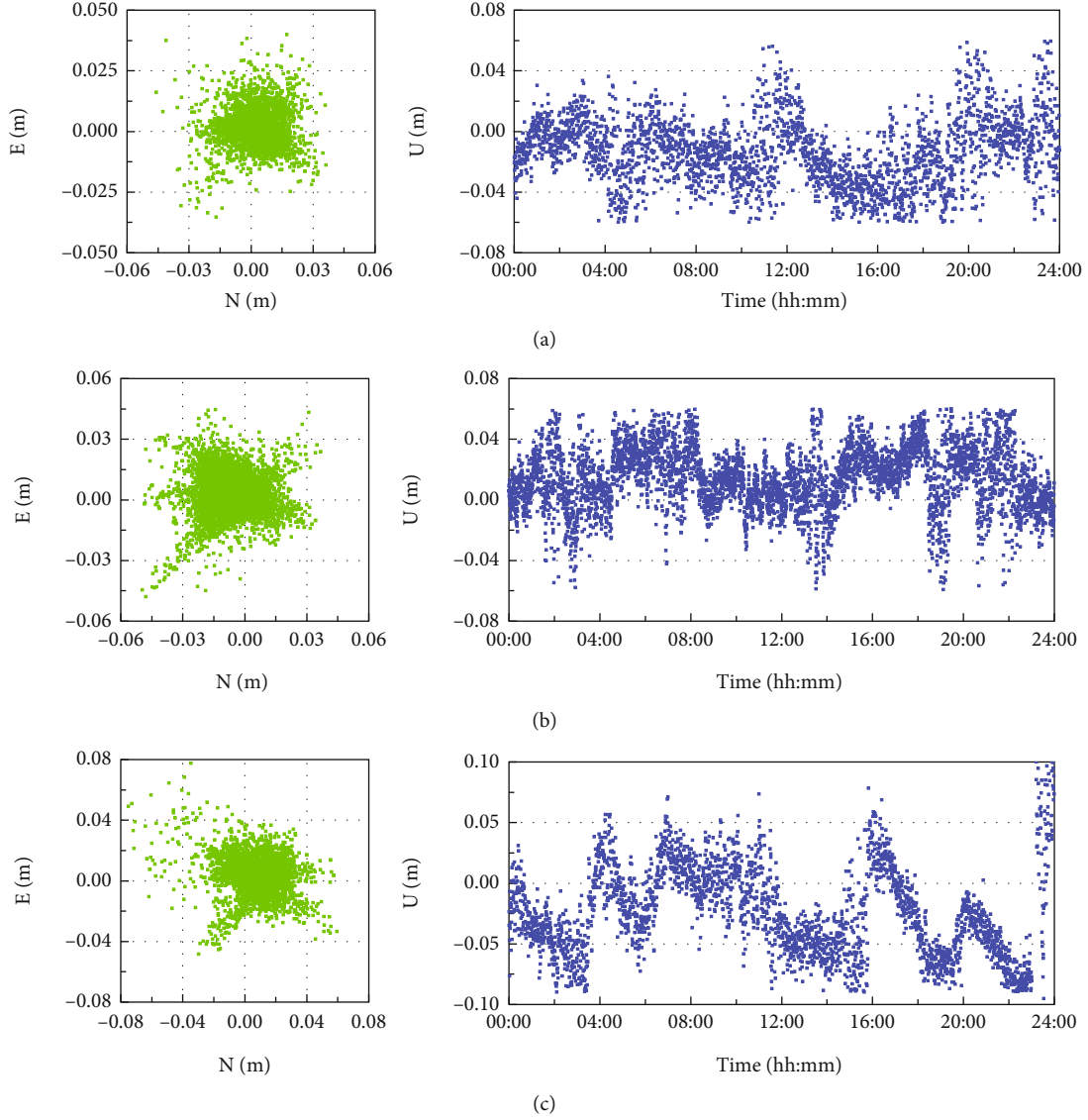
(a)

(b)

(c)

FIGURE 14: The positioning error series for the NL combination observations on datasets A, B, and C.

observation equations as follows:

$$
\begin{bmatrix}
v_1^G \\
v_{WL12}^G \\
v_{WL12}^C \\
v_{WL13}^C \\
v_{WL12}^E \\
v_{WL13}^E
\end{bmatrix}
=
\begin{bmatrix}
\mathbf{B}^G & -\mathbf{I} & \lambda_1^G \mathbf{I} \\
\mathbf{B}^G & \dfrac{f_1^G}{f_2^G}\mathbf{I} & 0 \\
\mathbf{B}^C & 0 & 0 \\
\mathbf{B}^C & 0 & 0 \\
\mathbf{B}^E & 0 & 0 \\
\mathbf{B}^E & 0 & 0
\end{bmatrix}
\begin{bmatrix}
\mathbf{X} \\
\mathbf{Ion}^G \\
\mathbf{N}^G
\end{bmatrix}
-
\begin{bmatrix}
\mathbf{l}_1^G \\
\mathbf{l}_{WL12}^G \\
\mathbf{l}_{WL12}^C \\
\mathbf{l}_{WL13}^C \\
\mathbf{l}_{WL12}^E \\
\mathbf{l}_{WL13}^E
\end{bmatrix},
$$

$$(9)$$

where $\mathbf{Ion}^G$ denotes the ionosphere delay vector of the GPS NL observation.

Equation (9) can be simplified to

$$v = \mathbf{AY} - \mathbf{l}, \tag{10}$$

where v denotes the observation residual matrix, $\mathbf{A}$ is the coefficient matrix of $\mathbf{Y}$, and $\mathbf{l}$ represents the OMC matrix. Set the weight matrix of the ionosphere parameters by $\mathbf{P}_G = (\Sigma_G)^{-1}$ and the corresponding vc-matrix by Σ_G. Afterwards, the least-squares solution is expressed as follows:

$$\hat{\mathbf{Y}} = (\mathbf{APA} + \mathbf{P}_c)^{-1}\mathbf{APL}. \tag{11}$$

The matrix $\mathbf{P}_G$ refers to the diagonal matrix with elements equal to $1/\sigma_G^2$, and σ_G^2 denotes the prior variance for ionosphere parameters.

If the WL ambiguity cannot be fixed, a higher-precision observation cannot be achieved. In this regard, the equivalent observations adopting triple-frequency

TABLE 6: Statistical results of single-epoch RTK-positioning error for NL observations (m).

Dataset	N	E	U
A	1.63	1.55	2.32
B	1.72	1.67	2.68
C	1.84	1.75	2.85

EWL observations of BDS and Galileo and NL carrier observations of GPS were jointly developed in this study as follows:

$$
\begin{bmatrix} v_{EWL1}^{C} \\ v_{EWL2}^{C} \\ v_{EWL1}^{E} \\ v_{EWL2}^{E} \\ v_{1}^{G} \end{bmatrix} = \begin{bmatrix} \mathbf{B}^{C} & \beta_{(0,-1,1)}^{C}\mathbf{I} & 0 \\ \mathbf{B}^{C} & \beta_{(1,4-5)}^{C}\mathbf{I} & 0 \\ \mathbf{B}^{E} & \beta_{(0,-1,1)}^{E}\mathbf{I} & 0 \\ \mathbf{B}^{E} & \beta_{(1,5,-6)}^{E}\mathbf{I} & 0 \\ \mathbf{B}^{G} & \mathbf{I} & \lambda_{1}^{G}\mathbf{I} \end{bmatrix} \begin{bmatrix} \mathbf{X} \\ \mathbf{Ion} \\ \mathbf{N}^{G} \end{bmatrix} - \begin{bmatrix} \mathbf{l}_{EWL1}^{C} \\ \mathbf{l}_{EWL2}^{C} \\ \mathbf{l}_{EWL1}^{E} \\ \mathbf{l}_{EWL2}^{E} \\ \mathbf{l}_{1}^{G} \end{bmatrix}.
$$

$$(12)$$

Figure 12 illustrates the multifrequency multisystem GNSS single-epoch RTK-positioning process. With the ambiguity fixed progressively, the accuracy of the RTK is also enhanced gradually. At the same time, the proposed method could ensure high positioning accuracy when the ARs of WL and NL failed.

As mentioned above, using the real data with different baseline lengths ranging from 22.41 m to 50.61 km to confirm the feasibility of the proposed approach and assess the NL AR fixed rate, two scenarios were designed as follows:

(1) Scenario 1: the first step was the GPS WL AR calculation using a GB model. In the second step, the NL ambiguities were fixed using the IF combination

(2) Scenario 2: the first step was the WL AR calculation for GPS, Galileo, and BDS systems using the GB model. Second, the ambiguity-fixed WL observations of Galileo, BDS, and GPS act as constraints, and the ionospheric delay is parameterized

Figure 13 illustrates the Ratio values for scenarios 1 and 2 across the three baselines. The fixed rates of the single-epoch NL ambiguities are listed in Table 5. As shown in Figure 13, the Ratio values for Scenario 2 are significantly larger compared to the values for Scenario 1, indicating a better-fixed rate of NL ambiguity for Scenario 2. In addition, as presented in Table 5, for Baseline A, at the Ratio threshold of 2, the fixed rate of the NL ambiguity for Scenario 2 was 96.32%, which was 26.1% higher than that for Scenario 1. For the 50 km baseline, the NL ambiguity-fixed rate for Scenario 1 was only 47.74% at the Ratio threshold of 2, which could not ensure the feasibility of single-epoch RTK positioning. When the proposed method was used, the fixed rate of NL ambiguity was still 93.26%, which could effectively ensure single-epoch RTK positioning.

To confirm the feasibility of the proposed approach, the positioning errors of the three baselines were calculated, as shown in Figure 14; the RMS values in the three directions are listed in Table 6. As shown in Figure 14, the three baseline errors were all below 0.08 m in horizontal directions and lower than 0.1 m in vertical directions. The RMS values in the 3 directions increased with the length of the baseline, and the maximal value was achieved in the vertical direction. For the 50 km baseline, the RMS values were better than 2 cm in the horizontal directions and approximately 2.9 cm in the vertical directions. As the critical factor affecting the fixed rate of NL ambiguity for medium-long baselines, double-difference ionospheric delay should be parameterized. Moreover, in this study, the ambiguity-fixed WL observations of the Galileo, BDS, and GPS observations were considered high-precision observations, which effectively elevated the NL ambiguity-fixed rate.

4. Conclusion

The narrow-lane (NL) observations of the GPS are subjected to the double-difference ionospheric delay for a medium-long baseline, which affects the fixed rate of ambiguity. To address this problem, this study proposes a single-epoch multifrequency multisystem real-time kinematic (RTK) modified method. First, the Galileo and BDS extra-wide-lane (EWL) ambiguities are fixed at a high success rate, and the Galileo and BDS WL ambiguity is solved by the transformation process. Second, the ambiguity-fixed WL is employed to upregulate the GPS WL ambiguity-fixed rate, and the parameterizing strategy of the ionospheric delay is adopted to enhance the rate of GPS NL ambiguity fixing. The feasibility of the proposed approach is verified by measured data. The conclusions of this study are listed below:

(1) The full operational capability (FOC) E5a/E5b can achieve an optimal performance at all frequencies; it is followed by the IIR-M L1, while the IIR-A/B L2 performs the worst. The FOC satellite is superior to the other two systems, which is mainly because of the application of advanced modulation schemes. The MPC of Galileo signals shows root mean square (RMS) data below 0.4 m with the following order: E 1 > E5b > E5a. In the BDS-2 system, the B3 signal exhibits an optimal performance, while the B1 signal performs the worst among all signals. For the GPS, RMS values of the MPC for the L2 signals are lower than those of the L1 signal

(2) At the Ratio value of 2, the fixed rate of the GPS WL ambiguity resolution assisted by the BDS/Galileo can reach a value over 95% for a medium-long baseline. The Galileo/BDS WL carrier observations, together with the fixed WL ambiguity of the BDS and Galileo systems, can enhance the constraints on position coordinates, which is conducive to elevating the fixed rate of the GPS WL AR

(3) In terms of the 50 km baseline, the NL integer ambiguity-fixed rate of the GPS using the

ionosphere-free (IF) combination is only 47.74% at the Ratio threshold of 2, which cannot ensure the feasibility of single-epoch RTK positioning. However, using the proposed method, the fixed rate of GPS NL ambiguity can reach 93.26%, which can further optimize both the positioning accuracy and the AR for a medium-long distance. Therefore, the proposed approaches broaden the future application of deformation monitoring in medium-long baseline scenarios

Data Availability

Detailed data of this study are available from the corresponding author, upon reasonable request.

Conflicts of Interest

The authors have no conflicts of interest to declare.

Acknowledgments

References

[1] L. Pan, X. Zhang, X. Li et al., "Satellite availability and point positioning accuracy evaluation on a global scale for integration of GPS, GLONASS, BeiDou and Galileo," *Advances in Space Research*, vol. 63, no. 9, pp. 2696–2710, 2019.

[2] Y. Liu, S. Ye, P. Jiang, W. Song, and Y. Lou, "Combining GPS + GLONASS observations to improve the fixing percentage and precision of long baselines with limited data," *Advances in Space Research*, vol. 57, no. 5, pp. 1258–1267, 2016.

[3] Y. Yuan, J. Li, A. Wang et al., "Preliminary assessment of the navigation and positioning performance of BeiDou regional navigation satellite system," *Science China Earth Sciences*, vol. 57, no. 1, pp. 144–152, 2014.

[4] X. Wang, X. Xu, and Q. Zhao, "Signal quality analysis and orbit accuracy verification of BDS-3," *Geomatics and Information Science of Wuhan University*, vol. 48, no. 4, pp. 611–619, 2023.

[5] F. Xia, S. Ye, P. Xia et al., "Assessing the latest performance of Galileo-only PPP and the contribution of Galileo to multi-GNSS PPP," *Advances in Space Research*, vol. 63, no. 9, pp. 2784–2795, 2019.

[6] N. Zhu, J. Marais, D. Betaille, and M. Berbineau, "GNSS position integrity in urban environments: a review of literature," *IEEE Transactions on Intelligent Transportation Systems*, vol. 19, no. 9, pp. 2762–2778, 2018.

[7] J. Chen, P. Han, Y. Zhang, T. You, and P. Zheng, "Scheduling energy consumption-constrained workflows in heterogeneous multi-processor embedded systems," *Journal of Systems Architecture*, vol. 142, no. 12, article 102938, 2023.

[8] Z. Dong and S. Jin, "Evaluation of the land GNSS-reflected DDM coherence on soil moisture estimation from CYGNSS data," *Remote Sensing*, vol. 13, no. 4, p. 570, 2021.

[9] J. Chen, Y. Zhang, L. Wu, T. You, and X. Ning, "An adaptive clustering-based algorithm for automatic path planning of heterogeneous UAVs," *IEEE Transactions on Intelligent Transportation Systems*, vol. 23, no. 9, pp. 16842–16853, 2022.

[10] Y. Li, H. Yan, S. Wang, and W. Yang, "Fuzz clustering analysis method for optimal combinations of BDS triple-frequency signals," *Acta Geodaetica et Cartographica Sinica*, vol. 49, no. 9, pp. 974–982, 2020.

[11] J. Li, Y. Yuan, H. He, J. Xu, and H. Guo, "Optimal carrier-phase combinations for triple-frequency GNSS derived from an analytical method," *Acta Geodaetica et Cartographica Sinica*, vol. 41, no. 6, pp. 797–803, 2012.

[12] B. Forssell, M. Martin-Neira, and R. A. Harrisz, "Carrier phase ambiguity resolution in GNSS-2," in *Proceedings of the 10th International Technical Meeting of the Satellite Division of The Institute of Navigation (ION GPS 1997)*, pp. 1727–1736, Kansas City, Missouri, 1997.

[13] U. Vollath, S. Birnbach, H. Landau, J. M. Fraile-Ordonez, and M. Martin-Neira, "Analysis of three-carrier ambiguity resolution technique for precise relative positioning in GNSS-2," *Journal of The Institute of Navigation*, vol. 46, no. 1, pp. 13–23, 1999.

[14] J. Jung, P. Enge, and B. Pervan, "Optimization of cascade integer resolution with three civil GPS frequencies," in *Proceedings of the 13th International Technical Meeting of the Satellite Division of The Institute of Navigation (ION GPS 2000)*, pp. 2191–2200, Salt Lake City, Utah, 2000.

[15] P. Teunissen, P. Joosten, and C. Tiberius, "A comparison of TCAR, CIR and LAMBDA GNSS ambiguity resolution," in *Proceedings of the 15th International Technical Meeting of the Satellite Division of The Institute of Navigation (ION GPS 2002)*, pp. 2799–2808, Portland, Oregon, 2002.

[16] Y. Feng, "GNSS three carrier ambiguity resolution using ionosphere-reduced virtual signals," *Journal of Geodesy*, vol. 82, no. 12, pp. 847–862, 2008.

[17] K. Wang and M. Rothacher, "Ambiguity resolution for triple-frequency geometry-free and ionosphere-free combination tested with real data," *Journal of Geodesy*, vol. 87, no. 6, pp. 539–553, 2013.

[18] B. Li, Y. Feng, W. Gao, and Z. Li, "Real-time kinematic positioning over long baselines using triple-frequency BeiDou signals," *IEEE Transactions on Aerospace and Electronic Systems*, vol. 51, no. 4, pp. 3254–3269, 2016.

[19] Y. Wu, X. Fu, H. Li, and J. Liu, "Application of TCAR/MCAR method in different baseline ambiguity resolution," *Geomatics and Information Science of Wuhan University*, vol. 32, no. 2, pp. 172–175, 2007.

[20] W. Tang, C. Deng, C. Shi, and J. Liu, "Triple-frequency carrier ambiguity resolution for Beidou Navigation Satellite System," *GPS Solutions*, vol. 18, no. 3, pp. 335–344, 2014.

[21] B. Li, Y. Feng, and Y. Shen, "Three carrier ambiguity resolution: distance-independent performance demonstrated using semi-generated triple frequency GPS signals," *GPS Solutions*, vol. 14, no. 2, pp. 177–184, 2010.

[22] X. Zhang and X. He, "Performance analysis of triple-frequency ambiguity resolution with BeiDou observations," *GPS Solutions*, vol. 20, no. 2, pp. 269–281, 2016.

[23] Q. Zhao, Z. Dai, Z. Hu, B. Sun, C. Shi, and J. Liu, "Three-carrier ambiguity resolution using the modified TCAR method," *GPS Solutions*, vol. 19, no. 4, pp. 589–599, 2015.

[24] J. Li, Y. Yuan, H. He, and H. Guo, "Benefits of BDS-3 B1C/B1I/B2a triple-frequency signals on precise positioning and ambiguity resolution," *GPS Solutions*, vol. 24, no. 4, p. 100, 2020.

[25] A. Al-Shaery, S. Zhang, and C. Rizos, "An enhanced calibration method of GLONASS inter-channel bias for GNSS RTK," *GPS Solutions*, vol. 17, no. 2, pp. 165–173, 2013.

[26] J. Duan and Y. Shen, "An algorithm of combined GPS/GLONASS static relative positioning," *Geodaetica et Cartographica Sinica*, vol. 41, no. 3, pp. 825–830, 2012.

[27] E. Wang, W. Song, Y. Zhang et al., "Evaluation of BDS/GPS multi-frequency RTK positioning performance under different baseline lengths," *Remote Sensing*, vol. 14, no. 15, p. 3561, 2022.

[28] Y. Liu, Z. Gao, Q. Xu, Y. Li, and L. Chen, "Assessing partial ambiguity resolution and WZTD-constraint multi-frequency RTK in an urban environment using new BDS signals," *GPS Solutions*, vol. 26, no. 3, p. 88, 2022.

[29] C. Deng, W. Tang, J. Liu, and C. Shi, "Reliable single-epoch ambiguity resolution for short baselines using combined GPS/BeiDou system," *GPS Solutions*, vol. 18, no. 3, pp. 375–386, 2014.

[30] H. He, J. Li, Y. Yang, J. Xu, H. Guo, and A. Wang, "Performance assessment of single- and dual-frequency BeiDou/GPS single-epoch kinematic positioning," *GPS Solutions*, vol. 18, no. 3, pp. 393–403, 2014.

[31] P. Teunissen, R. Odolinski, and D. Odijk, "Instantaneous BeiDou+GPS RTK positioning with high cut-off elevation angles," *Journal of Geodesy*, vol. 88, no. 4, pp. 335–350, 2014.

[32] R. Odolinski, P. Teunissen, and D. Odijk, "Combined BDS, Galileo, QZSS and GPS single-frequency RTK," *GPS Solutions*, vol. 19, no. 1, pp. 151–163, 2015.

[33] W. Gao, C. Gao, and S. Pan, "A method of GPS/BDS/GLONASS combined RTK positioning for middle-long baseline with partial ambiguity resolution," *Survey Review*, vol. 49, no. 354, pp. 212–220, 2017.

[34] J. Wang and Y. Feng, "Reliability of partial ambiguity fixing with multiple GNSS constellations," *Journal of Geodesy*, vol. 87, no. 1, pp. 1–14, 2013.

[35] J. He, W. Liu, and X. Zhang, "Single epoch ambiguity resolution of BDS triple frequency measured data under short baseline," *Geomatics and Information Science of Wuhan University*, vol. 40, no. 3, pp. 361–365, 2015.

[36] S. Ji, W. Cheng, C. Zhao, X. Ding, and Y. Chen, "Single epoch ambiguity resolution for Galileo with the CAR and LAMBDA methods," *GPS Solutions*, vol. 11, no. 4, pp. 259–268, 2007.

[37] S. Ye, L. Zhao, D. Chen, X. Pan, Z. Du, and Z. Li, "Real-time deformation monitoring data processing based on BDS triple-frequency observations," *Geomatics and Information Science of Wuhan University*, vol. 41, no. 6, pp. 722–728, 2016.